ELSEVIER

Ceramics International 30 (2004) 1127–1133

CERAMICS INTERNATIONAL

www.elsevier.com/locate/ceramint

Nano-structured oxide semiconductor materials for gas-sensing applications

O.K. Tan*, W. Cao, Y. Hu, W. Zhu

Microelectronics Center, School of EEE, Nanyang Technological University, 50 Nanyang Avenue, Block S1, Singapore 639798, Singapore

Received 28 November 2003; accepted 18 December 2003

Available online 24 April 2004

Abstract

Several types of nano-structured metal oxide semiconductor materials have been successfully synthesized for the sensing of both ethanol and oxygen gases. Using the high-energy ball milling process, stable nano-particle powders down to a few nanometers can be achieved at room temperature. In the case of ethanol sensing, the α-Fe_2O_3–SnO_2, α-Fe_2O_3–ZrO_2, and α-Fe_2O_3–TiO_2 materials are investigated while for the oxygen sensing, the ZrO_2–α-Fe_2O_3, TiO_2–α-Fe_2O_3, and $SrTiO_3$ types are studied for different applications. All the nano-structured oxide materials are systematically characterized using XRD, TEM, and the fabricated sensor devices characterized for their electrical and sensing properties. The sensing properties are compared and analyzed and the sensing mechanisms are explained for the different type of sensing materials. The effects of the nano-structure on the sensing properties are investigated.

Keywords: Nano-structured; High-energy ball milling; Oxygen; Ethanol; Gas sensors

1. Introduction

In the current materials science research, the use of nano-sized materials for gas sensors is rapidly arousing interest in the scientific community. One reason is that the surface-to-bulk ratio for the nano-sized materials is much greater than that for coarse materials. Another reason is that the conduction type of the material is determined by the grain size of the material. When the grain size is small enough (the actual grain size D is less than two times the space-charge depth L), the material resistivity is determined by grain control, and the material conduction type becomes surface conduction type [1]. Hence, the grain-size reduction becomes one of the main factors in enhancing the gas-sensing properties of semiconducting oxides.

Normally, nano-sized powders have been prepared by sol–gel process [2,3], chemical co-precipitation [4], metalorganic decomposition (MOD) [5], plasma enhanced chemical vapor deposition (PECVD) [6], atmospheric-pressure chemical vapor deposition (APCVD) [7], physical vapor deposition (PVD) [8,9], low-pressure flame deposition (LPFD) [10], and laser ablation [11]. Besides the above methods, the high-energy ball milling or mechanical alloying [12] has been proved to be a very effective route in preparing nano-sized solid solution for gas-sensing application recently [13–17].

In this paper, the high-energy ball milling technique has been employed to synthesized various nanometer powders with an average particle size down to several nanometers, including (1) nano-sized α-Fe_2O_3 based solid solutions mixed with different mole percent of SnO_2, ZrO_2, and TiO_2 separately for ethanol gas-sensing application, (2) stabilized ZrO_2 based and TiO_2 based solid solutions mixed with different mole percent of α-Fe_2O_3, and (3) synthesized $SrTiO_3$ for oxygen gas-sensing application. The synthesized powders and their sensing properties have been characterized. Meanwhile, the sensing mechanisms have been presented.

2. Experimental

Various nano-sized materials were prepared by high-energy ball milling in a Fritsch pulverisette 5 planetary ball milling system for ethanol gas-sensing and oxygen gas-sensing applications (see Table 1). The powder samples were formed into paste and screen-printed onto ceramic substrates with inter-digital Au electrodes to obtain the gas sensors.

* Corresponding author. Tel.: +65-6790-5411; fax: +65-6791-2687.
E-mail address: eoktan@ntu.edu.sg (O.K. Tan).

0272-8842/$30.00
doi:10.1016/j.ceramint.2003.12.015

Table 1
Nano-structured sensing materials prepared by high-energy ball milling technique

For ethanol gas sensing	For oxygen gas sensing
Composition	
(1) $x$$ZrO_2$–$(1-x)$α-$Fe_2O_3$, $x = 0.05$, 0.10, 0.15, and 0.20	(1) xα-Fe_2O_3–$(1-x)$$ZrO_2$, $x = 0.05$, 0.10, 0.15, and 0.20
(2) $x$$SnO_2$–$(1-x)$α-$Fe_2O_3$, $x = 0$, 0.03, 0.064, and 0.10	(2) xα-Fe_2O_3–$(1-x)$$TiO_2$, $x = 0.20$
(3) $x$$TiO_2$–$(1-x)$α-$Fe_2O_3$, $x = 0.05$, 0.10, 0.15, and 0.20	(3) Synthesized $SrTiO_3$

The characteristics of the material powders were investigated by XRD and TEM. The powder samples with different composition taken at different milling times were characterized using a Rigaku RINT 2000 X-ray diffractometer with Cu Kα radiation at room temperature. X-ray 1.54056 Å of Cu Kα1 radiation at 40 kV 40 mA was chosen as the source in the range of $20^\circ \leq 2\theta \leq 60^\circ$ with a sweep rate of 1°/min (except for the synthesized $SrTiO_3$ material, a SHIMADZU XRD-6000 X-ray diffractometer with Cu Kαl radiation (1.54056 Å) at 50 kV 20 mA in the range of $10^\circ \leq 2\theta \leq 100^\circ$ with a sweep rate of 4°/min was used). The microstructures of the milled powders and heat-treated powders were studied using the Jeol JEM2010 Transmission Electron Microscope (TEM). The TEM specimens were prepared by scattering the fine powders in ethanol solution using ultrasonic vibration and then sprayed onto holey carbon films, before being dried in air.

The gas-sensing properties were characterized with a Keithley 236 source measurement unit in a custom-designed gas-sensing characterization system programmed with the National Instruments' LABVIEW version 5.0. The sensing mechanisms have been investigated.

3. Results and discussion

3.1. Mechanical alloying process

3.1.1. $0.10ZrO_2$–0.90α-Fe_2O_3 for ethanol sensing application

The XRD patterns of $0.10ZrO_2$–0.90α-Fe_2O_3 milled for different hours are shown in Fig. 1a, the positions of all the strong peaks were found to correspond to those of the α-Fe_2O_3. Even after 120-h milling, those peaks can still be distinguished. However no peaks corresponding to those of pure ZrO_2 (labeled as ZrO_2 in 0-h curve) were found. This indicated that the basic structure of hematite for all the milled powder samples remained the same as that of the starting material of α-Fe_2O_3, i.e., the corundum structure. The particle size decreased drastically to less than 10 nm after 20 h of milling and remains about the same up to 120 h of milling in Fig. 1b (calculated by *Scherrer* formula [12]). Similar trend was observed for all the other powders listed in Table 1. The results also were confirmed by TEM [18].

In order to clarify the effect on the crystal structure of the milled powders, the lattice refinements from the X-ray diffraction patterns were performed for the powders with different mole percents of ZrO_2 and different milling times. Fig. 2a and b shows the increase of both a and c axes of the hexagonal cell with increasing milling time. The lattice constants of the 120-h milled $x$$ZrO_2$–$(1-x)$α-$Fe_2O_3$ samples also increase with increasing ZrO_2 content x, from $a = 0.5038$ nm and $c = 1.3772$ nm for $x = 0$ (pure α-Fe_2O_3) to $a = 0.5060$ nm and $c = 1.3900$ nm for $x = 0.20$. Similar observations for $x$$SnO_2$–$(1-x)$α-$Fe_2O_3$ were also reported [19].

This result can be explained using the non-equilibrium structural model that has proposed initially for $x$$SnO_2$–$(1-x)$α-$Fe_2O_3$ [19]. It was also found to be applicable to the $x$$ZrO_2$–$(1-x)$α-$Fe_2O_3$ system [13]. To apply this model to the material system of $x$$ZrO_2$–$(1-x)$α-$Fe_2O_3$, the structural model can be expressed in the form of Kröger–Vink notation as:

$$ZrO_2 \rightarrow Zr_i^{\bullet\bullet\bullet\bullet} + 2O_S'' \quad (1)$$

$$O_S'' \rightarrow O_S' + e' \quad (2)$$

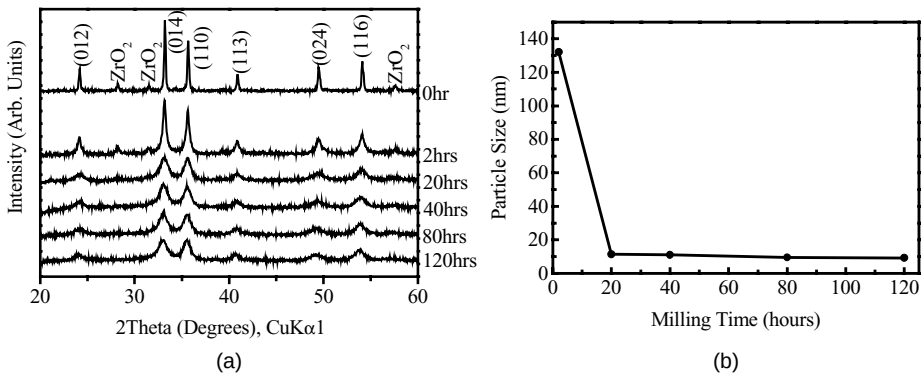

Fig. 1. (a) XRD patterns and (b) average particle size of $0.10ZrO_2$–0.90α-Fe_2O_3 milled for different milling hours.

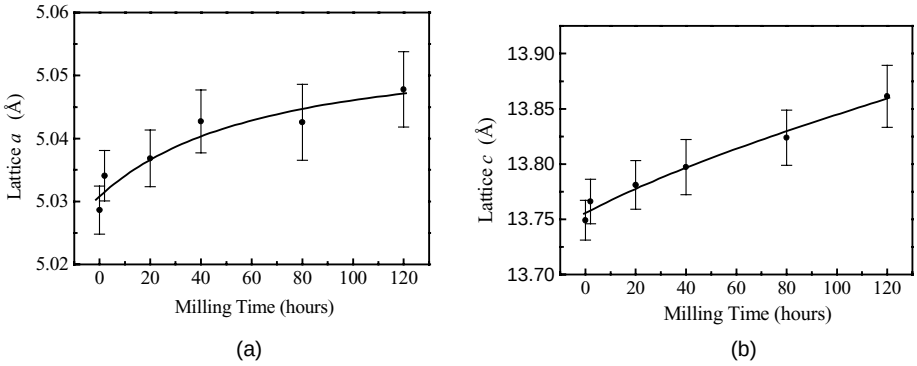

Fig. 2. Lattice constant for $0.10ZrO_2$–0.90α-Fe_2O_3 powder versus milling times: (a) *a* and (b) *c*.

$$2O'_S \rightarrow O_2 + 2e' \quad (3)$$

The corundum structure of α-Fe_2O_3 is depicted in Fig. 3. The O^{2-} ions form the hexagonal close-packed (HCP) lattice with two Fe^{3+} ions alternatively occupying the three available octahedral sites (i.e., 2/3 of the octahedral sites are occupied, and 1/3 are empty). In this model, the Zr^{4+} ions alternately occupy the 1/3 available site at the c_i plane with a certain probability and within the limit of the phase stability. At the same time, O^{2-} (O'') and O^- (O') ions are generated at the particle surfaces as given in Eqs. (1) and (2). This non-equilibrium structural model adequately provides an account for the sensing mechanism of $xZrO_2$–$(1-x)\alpha$-Fe_2O_3 ethanol gas sensor in Section 3.2.

3.1.2. 0.20α-Fe_2O_3–0.80ZrO_2 for oxygen sensing application

0.20α-Fe_2O_3–$0.80ZrO_2$ is a typical alloyed material for oxygen sensing application. The alloying process, for the 0.2α-Fe_2O_3–$0.8ZrO_2$ milled for different hours, was investigated to reveal the sensing mechanism.

Fig. 4 shows the X-ray diffraction patterns of these milled powders. It presents the peaks of crystalline monoclinic ZrO_2 and corundum α-Fe_2O_3. For samples with 2-h milling, these main peaks did not shift, but their intensities were reduced due to the peak broadening. This indicates that the basic structure remained unchanged, only the reduction of the grain size had occurred during the first 2 h of milling. After a milling time of 20 h, the three main peaks of cubic ZrO_2 (1 1 1), (2 0 0), and (2 2 0), in the 2θ range of 20–60°, can be observed. With further milling to 60 h, the peaks of monoclinic ZrO_2 and corundum α-Fe_2O_3 disappeared completely. There was no significant change in the XRD peaks with further milling. With prolonged hours of milling, the impact energies derived are more than sufficient to force the iron ions into the zirconia structure and transform the phase from monoclinic to cubic.

The microstructure change during the alloying process was further investigated using TEM. Fig. 5a and b shows the morphology and Selected Area Diffraction (SAD) pattern of the powders milled after 2 and 120 h, respectively, as a typical observation. For particles milled for 2 h, most of the particle sizes were reduced down to about 25 nm. The SAD in Fig. 5a clearly shows two sets of diffraction rings for the monoclinic ZrO_2 and corundum α-Fe_2O_3 structure, respectively. For the powder milled for 120 h, no sign of individual particle from the bright-field image could be found in Fig. 5b, not even at the thin edges of the sample. These particles were difficult to be dispersed by ultrasonic vibration during TEM specimen preparation. They conglomerated together and formed a large lump. In Ref. [14], we postulated that these nano-particles are glued together in an amorphous-like matrix. This is supported by the selected

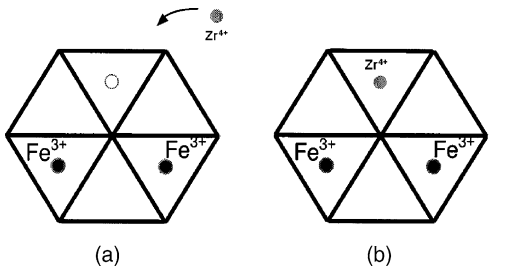

Fig. 3. The corundum structure for: (a) pure α-Fe_2O_3 and (b) mechanically alloyed $xZrO_2$–$(1-x)\alpha$-Fe_2O_3.

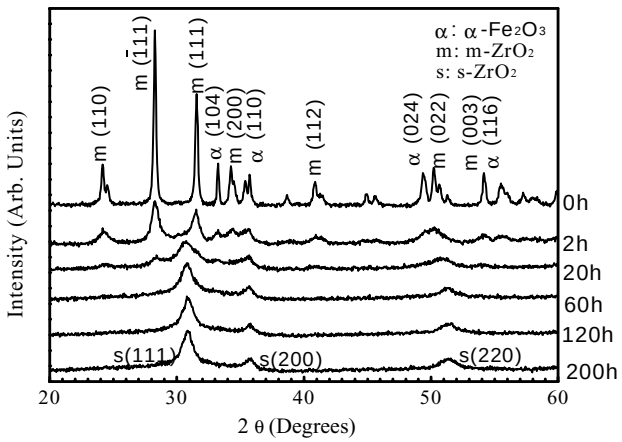

Fig. 4. X-ray diffraction patterns for samples, 0.20α-Fe_2O_3–$0.80ZrO_2$, milled for different times.

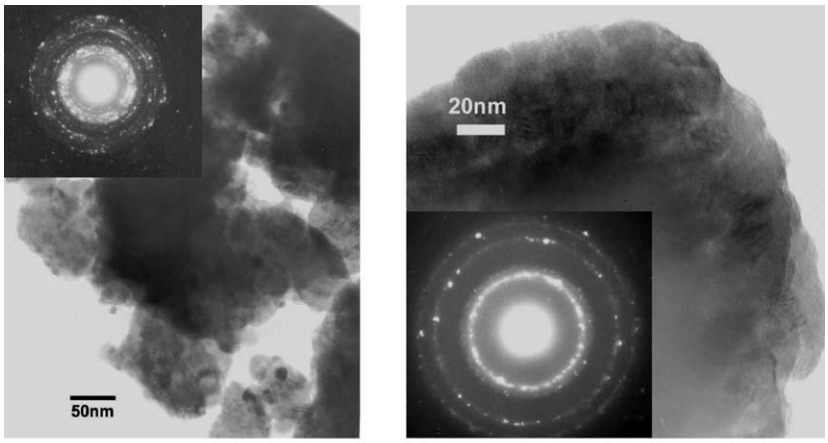

Fig. 5. TEM bright-field image and SAD pattern for the $0.2\alpha\text{-}Fe_2O_3$–$0.8ZrO_2$ powder milled for different hours: (a) 2 h, (b) 120 h.

area electron diffraction (Fig. 5b) as it gives a clear amorphous diffraction ring in addition to the diffraction rings of cubic ZrO_2. Hence, the powder milled after 120 h has an amorphous-like morphology. Moreover, no diffraction point belonging to $\alpha\text{-}Fe_2O_3$ particles can be detected. The substitution model [20–31] can be used to explain the dissolution of the Fe_2O_3 in the cubic ZrO_2 phase given by:

$$Fe_2O_3 \rightarrow 2Fe'_{Zr} + V_O^{\bullet\bullet} + 3O_O \quad (4)$$

The thermal stability of the milled $0.2\alpha\text{-}Fe_2O_3$–$0.8ZrO_2$ has been studied [13]. It was found that Fe^{3+} ions were expelled as $\alpha\text{-}Fe_2O_3$ from the cubic ZrO_2 above 650 °C. With the thermal reverse decomposition process, the substitution model can be further modified as:

$$Fe_2O_3 \rightleftarrows 2Fe'_{Zr} + V_O^{\bullet\bullet} + 3O_O \quad (5)$$

The variation of particle size with the milling time had been obtained from the TEM observation. The result was found to be similar to that shown in Fig. 1.

3.1.3. *Synthesized $SrTiO_3$ for oxygen sensing application*

Fig. 6 shows the XRD patterns for the synthesized $SrTiO_3$ samples after different milling times. After 20 h, the $SrTiO_3$ structure material, a cubic perovskite phase, was distinctive, and at 120 h, the average grain size of 20 nm powders were obtained (calculated by *Scherrer* formula [12]).

The grain size and perovskite crystal structure of synthesized $SrTiO_3$ were also observed using TEM as shown Fig. 7. Both characterization showed consistent results.

3.2. *Gas-sensing properties and mechanisms*

In this section, the gas-sensing properties of nano-sized solid solutions were characterized for ethanol gas sensing and oxygen gas sensing, respectively. For these resistive-type semiconducting oxide based gas sensors, the relative resistance R/R_0 [32] is used to express the sensor response to the test gas. For ethanol gas sensors, R_0 is the resistance of the

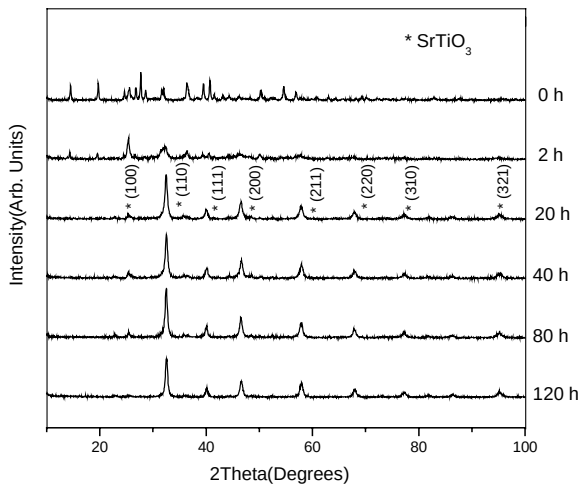

Fig. 6. XRD patterns for synthesized $SrTiO_3$ samples for different milling times.

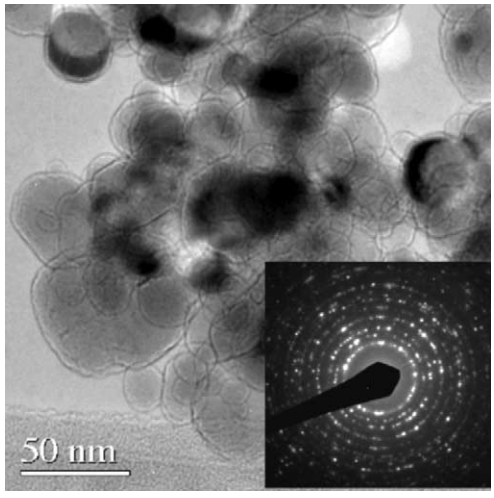

Fig. 7. TEM bright-field image and SAD pattern of synthesized $SrTiO_3$ powders milled for 120 h.

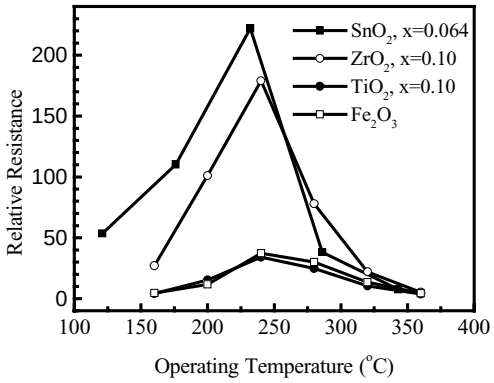

Fig. 8. Relative resistance in 100 ppm of ethanol gas in air versus operating temperature for sensors of $0.064SnO_2$–0.936α-Fe_2O_3, $0.10ZrO_2$–0.90α-Fe_2O_3, $0.10TiO_2$–0.90α-Fe_2O_3 and pure α-Fe_2O_3.

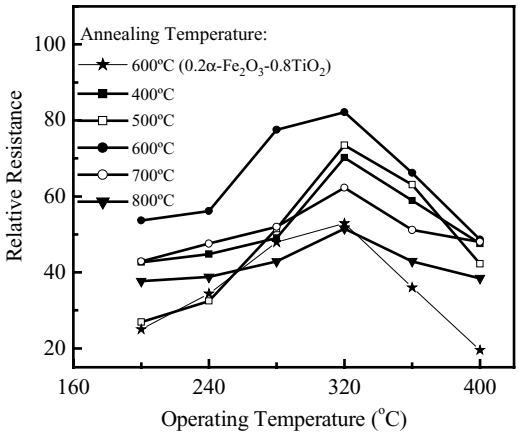

Fig. 9. Relative resistance of 0.2α-Fe_2O_3–$0.8ZrO_2$ for different annealing temperatures and operating temperatures.

sensor in ethanol and R is the resistance of the sensor in air. For oxygen gas sensors, R_0 is the resistance of the sensor in nitrogen and R is the resistance of the sensor in different concentration oxygen gas diluted by nitrogen.

3.2.1. Ethanol gas sensing

The three types of solid solutions, $x$$SnO_2$–$(1-x)\alpha$-$Fe_2O_3$, $x$$ZrO_2$–$(1-x)\alpha$-$Fe_2O_3$, and $x$$TiO_2$–$(1-x)\alpha$-$Fe_2O_3$, have been investigated for ethanol gas-sensing application. The relative resistances for the optimum compositions in each type of solid solutions and pure α-Fe_2O_3 were compared in Fig. 8. All these four samples, $0.10ZrO_2$–0.90α-Fe_2O_3, $0.064SnO_2$–0.936α-Fe_2O_3, $0.10TiO_2$–0.90α-Fe_2O_3, and pure α-Fe_2O_3, were ball milled for 120 h and annealed at 400 °C in air for 1 h. It was found that the relative resistance values of $0.064SnO_2$–0.936α-Fe_2O_3 ethanol gas sensor and $0.10ZrO_2$–0.90α-Fe_2O_3 ethanol gas sensor to 100 ppm of ethanol gas were about six to eight times that of $0.10TiO_2$–0.90α-Fe_2O_3 ethanol gas sensor. The relative resistance values of $0.10TiO_2$–0.90α-Fe_2O_3 ethanol gas sensor are also the same as that of pure α-Fe_2O_3 at different operating temperatures.

The non-equilibrium structural model for milled $x$$SnO_2$–$(1-x)\alpha$-$Fe_2O_3$ and $x$$ZrO_2$–$(1-x)\alpha$-$Fe_2O_3$ has been elucidated [13,19]. Based on the XRD study, it is believed that this model is also applicable to $x$$TiO_2$–$(1-x)\alpha$-$Fe_2O_3$. These nano-sized particles have large surface area and are in a non-equilibrium state. When the ethanol gas is introduced, it reacts with the O_2 at the particle surface. The depletion of O_2 causes the Eqs. (2) and (3) to shift to the right and extra electrons are generated. This increases the conductivity tremendously, and enhances the gas-sensing properties of α-Fe_2O_3 based gas sensors. However, in the case of $0.10TiO_2$–0.90α-Fe_2O_3 gas sensor, it is well known that titanium have different valence states. The quadrivalent titanium interacts with electrons and becomes trivalence titanium easily [29] as follows:

$$Ti^{4+} + e' \rightleftarrows Ti^{3+} \quad (6)$$

Due to this interaction, the extra electrons generated in Eqs. (2) and (3) will be counterbalanced by the depletion of electrons in Eq. (6) for the $0.10TiO_2$–0.90α-Fe_2O_3 system. As a result, the relative resistance values of $0.10TiO_2$–0.90α-Fe_2O_3 gas sensors remain the same as that of pure α-Fe_2O_3 gas sensor as shown in Fig. 8.

3.2.2. Oxygen gas sensing

The effect on the relative resistance in 20% of oxygen for the different annealing temperatures was characterized. The thick film devices of 0.2α-Fe_2O_3–$0.8ZrO_2$ were annealed for 1 h in air at 400, 500, 600, 700, and 800 °C, respectively. The relative resistances of these samples at different operating temperatures were plotted in Fig. 9. The optimal relative resistance of 82 was obtained from the sample annealed at 600 °C and operating at 320 °C. The samples annealed at different temperatures had a same optimal operating temperature at 320 °C. At this low operating temperature of 320 °C, the relative resistance increases with the increase of annealing temperatures between 400 and 600 °C. Beyond 600 °C, the relative resistance decreases with increasing annealing temperatures. According to the substitution and decomposition model given in Eq. (5), $Fe_2O_3 \rightleftarrows 2Fe'_{Zr} + V_O^{\bullet\bullet} + 3O_O$, $V_O^{\bullet\bullet}$ decreases with increasing annealing temperatures above 600 °C because of the decomposition above 650 °C [14]. Hence, the relative resistance decreases for annealing temperature above 650 °C.

Besides $x\alpha$-Fe_2O_3–$(1-x)ZrO_2$, 0.20α-Fe_2O_3–$0.80TiO_2$ milled for 120 h was also investigated for oxygen gas-sensing application. It showed the similar property of lower operating temperature at 320 °C in Fig. 9. More systematic works is being carried out for low-temperature oxygen gas sensing.

For the synthesized $SrTiO_3$ sensors, the effect of different annealing temperatures on the sensing property to 20% of oxygen was studied in Fig. 10. The thick film devices of the synthesized $SrTiO_3$ (milling 120 h) were annealed for 1 h in air at 400, 500, 600, 700, and 800 °C, respectively. The devices of the synthesized $SrTiO_3$ (annealing at 800 °C) is an

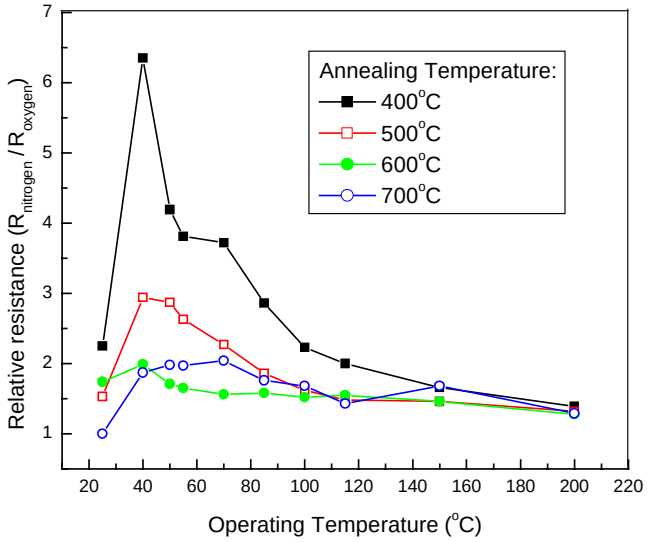

Fig. 10. Relative resistance of the synthesized $SrTiO_3$ sensors for different annealing temperature.

insulator and exhibits no sensing property. The other devices relative resistances with different annealing temperature at different operating temperatures were plotted in Fig. 10. The optimal relative resistance ($R_{nitrogen}/R_{oxygen}$) value of 6.35 was obtained for the pure synthesized $SrTiO_3$ sample annealed at 400 °C and operating at 40 °C. This value is comparable to the reported relative resistance of doped $SrTiO_3$ series oxygen gas sensors with operating temperature at 700–800 °C [33–35]. The figure also showed that most of the samples annealed at different temperatures had the same optimal operating temperature of 40 °C. This optimal operating temperature is much lower than that of the normal low-temperature metal oxide semiconducting oxygen gas sensors (300–500 °C) [36–39] and $SrTiO_3$ oxygen gas sensors (>700 °C) [40]. The annealing temperature only affects the grain size of the synthesized nano-sized $SrTiO_3$ material but does not change its perovskite structure as depicted in our XRD results [41]. The sensing properties of sensor device decrease with annealing temperature due to the grain size of the material increasing with annealing temperature. At annealing temperature above 800 °C, the grain size grows very large and the material resistivity of the device changes from grain control type to neck control type. It becomes an insulator and loses its sensing property [1].

4. Conclusions

High-energy ball milling technique has been employed to synthesize various nano-structured metal oxide semiconductor materials with average particle size down to several nanometers for gas-sensing applications. The mechanical alloying processes for both ethanol sensing materials and oxygen sensing materials have been investigated thoroughly to study the sensing mechanisms. Nano-sized α-Fe_2O_3 based solid solutions mixed with different mole percent of SnO_2, ZrO_2, and TiO_2 separately have been obtained and fabricated into thick film sensor devices for ethanol gas-sensing application. The optimal compositions, $0.064SnO_2$–0.936α-Fe_2O_3 and $0.10ZrO_2$–0.90α-Fe_2O_3, exhibit excellent sensing properties to ethanol gas. The sensing mechanism has been elucidated using a non-equilibrium structural model. On the other hand, the lower relative resistance for $x TiO_2$–$(1-x)\alpha$-Fe_2O_3 ethanol gas sensor has been explained by the different valence states of titanium. In the case of oxygen sensing application, stabilized zirconia based, TiO_2 based solid solutions mixed with different mole percent of α-Fe_2O_3 and $SrTiO_3$ are synthesized as the sensing materials. The different operating temperatures of 320 °C for 0.2α-Fe_2O_3–$0.8ZrO_2$ and 0.20α-Fe_2O_3–$0.80TiO_2$, and 40 °C for synthesized $SrTiO_3$ make them useful for different applications. Their sensing mechanisms have been also studied. All the results have shown that the high-energy ball milling is a very effective route to prepare nano-structured solid solutions at room temperature for gas-sensing applications.

References

[1] C. Xu, J. Tamaki, N. Miura, N. Yamazor, Grain size effects on gas sensitivity of porous SnO_2-based elements, Sens. Actuators B 3 (1991) 147–155.
[2] X.Q. Liu, S.W. Tao, Y.S. Shen, Preparation and characterization of nanocrystalline of αFe_2O_3 by a sol-gel process, Sens. Actuators B 40 (1997) 161–165.
[3] A.M. Taurino, M. Epifani, T. Toccoli, S. Iannotta, P. Siciliano, Innovative aspects in thin film technologies for nanostructured materials in gas sensor devices, Thin Solid Films 436 (2003) 52–63.
[4] Y. Nakatani, M. Matsuoka, Effects of sulfate ion on gas sensitive properties of αFe_2O_3 ceramics, Jpn. J. Appl. Phys. 21 (1982) 1758–1762.
[5] S. Xue, W. Ousi-Benomar, R.A. Lessard, αFe_2O_3 thin films prepared by metalorganic deposition (MOD) from Fe (III) 2-ethylhexanoate, Thin Solid Films 250 (1994) 194–201.
[6] Y. Liu, W. Zhu, O.K. Tan, Y. Shen, Structural and gas sensing properties of ultrafine Fe_2O_3 prepared by plasma enhanced chemical vapor deposition, Mater. Sci. Eng. B 47 (1997) 171–176.
[7] C.C. Chai, J. Peng, B.P. Yan, Preparation and gas sensing properties of alpha-Fe_2O_3 thin films, J. Electron. Mater. 24 (1995) 799–804.
[8] F. Edelman, et al., E-gun sputtered and reactive ion sputtered TiO_2 thin films for gas sensors, Inst. Electron Technol. 33 (2000) 89–107.
[9] M. Ferroni, et al., Nanosized thin films of tungsten–titanium mixed oxides as gas sensors, Sens. Actuators B 58 (1999) 289–294.
[10] F. Cosandey, G. Skandan, A. Singhal, Materials and processing issues in nanostructured semiconductor gas sensors, J. Mater. Sci. Mater. Electron. 52 (10) 2000.
[11] G. Williams, G.S.V. Cole, The gas-sensing potential of nanocrystalline tin dioxide produced by a laser ablation technique, MRS Bull. 24 (6) (1999) 25–29.
[12] L. Lü, M.O. Lai, Mechanical Alloying, Kluwer Academic Publishers, 1998, pp. 11–21.
[13] O.K. Tan, W. Cao, W. Zhu, Alcohol sensor based on a non-equilibrium nanostructured $xZrO_2$–$(1-x)\alpha$-Fe_2O_3 solid solution system, Sens. Actuators B 63 (1–2) (2000) 129–134.

[14] W. Cao, O.K. Tan, W. Zhu, B. Jiang, Mechanical alloying and thermal decomposition of $(ZrO_2)_{0.8}$–$(\alpha\text{-}Fe_2O_3)_{0.2}$ powder for gas sensing applications, J. Solid State Chem. 155 (2000) 320–325.
[15] J.Z. Jiang, S.W. Lu, Y.X. Zhou, S. Mϕrup, K. Nielsen, E.W. Poulsen, F.J. Berry, J. McMannus, Correlation of gas sensitive properties with Fe_2O_3–SnO_2 ceramic microstructure prepared by high energy ball milling, Mater. Sci. Forum 235–238 (1997) 941–946.
[16] J.Z. Jiang, R. Lin, W. Lin, K. Nielsen, S. Mϕrup, K. Dam-Johansen, R. Clasen, Gas sensitive properties and structure of nanostructured $(\alpha Fe_2O_3)_x$–$(SnO_2)_{1-x}$ materials prepared by mechanical alloying, J. Phys. D Appl. Phys. 30 (1997) 1459–1467.
[17] W. Cao, O.K. Tan, W. Zhu, B. Jiang, J.S. Pan, The study of $x\alpha\text{-}Fe_2O_3$–$(1-x)ZrO_2$ solid solution for resistive low temperature oxygen gas sensors, IEEE Sensors J. 3 (4) (2003) 421–434.
[18] W. Cao, Semiconductor oxide based gas sensors, Thesis submitted to Nanyang Technological University for Doctor of Philosophy, 2001, pp. 39–42.
[19] W. Zhu, O.K. Tan, J.Z. Jiang, A new model and gas sensitivity of non-equilibrium $xSnO_2$–$(1-x)\alpha Fe_2O_3$ nanopowders prepared by mechanical alloying, J. Mater. Sci. Mater. Electron. 9 (1998) 275–278.
[20] J.Z. Jiang, F.W. Poulsen, S. Mϕrup, Structure and thermal stability of nanostructured iron-doped zirconia prepared by high-energy ball milling, J. Mater. Res. 14 (1999) 1343.
[21] O.M. Zacate, L. Minervini, D.J. Bradfield, R.W. Rrimes, K.E. Sichafus, Defect cluster formation in M_2O_3-doped cubic ZrO_2, Solid State Ionics 128 (2000) 243–254.
[22] G. Chiodelli, G. Flor, M. Scagliotti, Electrical properties of the ZrO_2–CeO_2 system, Solid State Ionics 91 (1996) 109.
[23] K. Sasaki, J. Claus, J. Maier, Defect chemistry of oxides in partially frozen-in states: case studies for $ZrO_2(Y_2O_3)$, $SrZrO_3(Y_2O_3)$, and $SrTiO_3$, Solid State Ionics 121 (1999) 51–60.
[24] K. Sasaki, J. Maier, Re-analysis of defect equilibria and transport parameters in Y_2O_3-stabilized ZrO_2 using EPR and optical relaxation, Solid State Ionics 134 (2000) 303–321.
[25] M. Weller, H. Schubert, Internal friction, dielectric loss, and ionic conductivity of tetragonal ZrO_2-3%Y_2O_3 (Y-TZP), J. Am. Ceram. Soc. 69 (7) (1986) 573–577.
[26] P.S. Manning, J.D. Sirman, R.A. De Souza, J.A. Kilner, The kinetics of oxygen transport in 9.5 mol% single crystal yttria stabilized zirconia, Solid State Ionics 100 (1997) 1–10.
[27] J.F. Baumard, P. Abelard, Defect structure and transport properties of ZrO_2-based solid electrolytes, in: N. Claussen, M. Ruhle, A.H. Heuer (Eds.), Advances in Ceramics, Vol. 12, Science and Technology of Zirconia II, American Ceramic Society, Columbus, OH, 1984, pp. 555–571.
[28] P. Mondal, A. Klein, W. Jaegermann, H. Hahn, Enhanced specific grain boundary conductivity in nanocrystalline Y_2O_3-stabilized zirconia, Solid State Ionics 118 (1999) 331–339.
[29] D.M. Smyth, The effects of dopants on the properties of metal oxides, Solid State Ionics 129 (2000) 5–12.
[30] E.C. Subbarao, Zirconia—an overview, in: A.H. Heuer, L.W. Hobbs (Eds.), Advances in Ceramics, Vol. 3, Science and Technology of Zirconia I, American Ceramic Society, Columbus, OH, 1981, pp. 1–24.
[31] P. Li, I.-W. Chen, E. James, P. Hahn, Effect of dopants on zirconia stabilization—an X-ray absorption study: I. Trivalent dopants, J. Am. Ceram. Soc. 77 (1) (1994) 118–128.
[32] A. D'Amico, C.D. Natale, A contribution on some basic definitions of sensors properties, IEEE Sens. J. 1 (2001) 183–190.
[33] X.H. Zhou, O.T. Sørensen, Y.L. Xu, Defect structure and oxygen sensing properties of Mg-doped $SrTiO_3$ thick film sensors, Sens. Actuators B 41 (1997) 177–182.
[34] X. Zhou, O.T. Sørensen, Q. Cao, Y. Xu, Electrical conduction and oxygen sensing mechanism of Mg-doped $SrTiO_3$ thick film sensors, Sens. Actuators B 65 (2000) 52–54.
[35] H. Zheng, O.T. Sørensen, Integrated oxygen sensors based on Mg-doped $SrTiO_3$ fabricated by screen-printing, Sens. Actuators B 65 (2000) 299–301.
[36] Y.L. Xu, X.H. Zhou, O.T. Sørensen, Oxygen sensors based on semiconducting metal oxides: an overview, Sens. Actuators B 65 (2000) 2–4.
[37] G. Sberveglieri, Recent developments in semiconducting thin-film gas sensors, Sens. Actuators B 23 (1995) 103–109.
[38] P.T. Moseley, Materials selection for semiconductor gas sensors, Sens. Actuators B 6 (1992) 149–156.
[39] H. Meixner, U. Lampe, Metal oxide sensors, Sens. Actuators B 33 (1996) 198–202.
[40] W. Menesklou, H.-J. Schreiner, K.H. Hardtl, E. Ivers-Tiffee, High temperature oxygen sensors based on doped $SrTiO_3$, Sens. Actuators B 59 (1999) 184–189.
[41] Y. Hu, O.K. Tan, W. Cao, W. Zhu, Fabrication and characterization of $SrTiO_3$ oxygen sensor operating at very low temperature, in: The Second IEEE International Conference on Sensors (IEEE Sensors 2003), Toronto, Canada, 21–24 October, 2003, pp. 462–463.